

On the thermal stability of transonic accretion discs

Ewa Szuszkiewicz^{1,2} and John C. Miller^{2,3}

¹Astronomy Group, Department of Physics and Astronomy,
University of Leicester, University Road,
Leicester LE1 7RH, England

²International School for Advanced Studies, SISSA,
via Beirut 2-4, I-34013 Trieste, Italy

³Nuclear and Astrophysics Laboratory, University of Oxford,
Keble Road, Oxford OX1 3RH, England

Accepted for publication in the MNRAS (January 1997)

Abstract

Nonlinear time-dependent calculations have been carried out in order to study the evolution of the thermal instability for vertically integrated, non self-gravitating models of optically thick, transonic, slim accretion discs around black holes. In these calculations we investigated only the original version of the slim disc model with low viscosity ($\alpha = 0.001$) and for a stellar mass ($10 M_{\odot}$) black hole. This original version of the model does not yet include several important non-local effects (viscous forces in the radial equation of motion, diffusion-type formulation for the viscosity in the angular momentum equation, viscous dissipation rate associated with the stress in the azimuthal direction and radiative losses in the radial direction in the energy balance equation). It is clear, therefore, that this treatment is greatly simplified but our strategy is to consider this as a standard reference against which to compare results from forthcoming studies in which the additional effects will be added one by one thus giving a systematic way of understanding the contribution from each of them.

We have considered an already-formed disc and studied its stability against small axisymmetric perturbations. Those models which were stable according to local analysis, remain stable and stationary to a good approximation as also do models for which local analysis predicted an unstable region with radial dimension smaller than the shortest wavelength of the unstable modes. In terms of luminosity, all models with luminosity less than or equal to $0.08L_E$ are stable. For models with higher luminosity than this but which are still sub-Eddington, a shock-like structure forms near to the sonic point, probably leading to subsequent disruption of the disc. The model with Eddington luminosity evolves in a violent way, with the shock-like structure being formed already within the first second of evolution. From an examination of phase space trajectories, our preliminary conclusion is that the stabilizing effect of advection is not strong enough in these models to allow for limit cycle behaviour to occur. However, in order to make a definitive statement on this, it would be necessary to implement special numerical techniques for treatment of the shock-like structure, which becomes very extreme, and this lies beyond the scope of the present paper.

Subject headings: accretion: accretion discs, instabilities: thermal

1 Introduction

Accretion discs around black holes are thought to be present in galactic black hole candidates and active galactic nuclei. One of the characteristic properties of these objects is their variability. Apart from fundamental questions concerning the very existence of fluid disc-like configurations and their lifetimes, the most immediate purpose of the study of accretion disc stability is to discover the origin of the incipient instabilities which may be responsible for the observed variability. However, before applying the results of stability studies to realistic objects, one must eliminate the possibility that the behaviour of the model is merely a consequence of the approximations made in its construction (Piran, 1978; Pringle, 1981).

Equilibrium models of geometrically *thin* accretion discs were found to be subject to two types of instability – thermal (Pringle, Rees, and Pacholczyk, 1973) and viscous (Lightman and Eardley, 1974). A thorough investigation of these was carried out by Shakura and Sunyaev (1976) who found that the instabilities develop via a bifurcation of unstable modes. Both types of instability occur when radiation provides a substantial contribution to the total pressure. In thin discs, the thermal time scales are generally much shorter than the viscous ones and so thermal instabilities, if present, dominate over viscous instabilities. The first discussions of this were made in terms of local linear analysis, in which the global response of the disc and nonlinear effects were not taken into account, but then Lightman (1974) carried out time-dependent calculations to examine the global behaviour. Detailed time-dependent disc evolution was studied first in the context of dwarf novae (Meyer and Meyer-Hofmeister, 1982; Smak, 1982; Papaloizou, Faulkner and Lin, 1983). These authors showed that the dwarf nova outbursts arise from collective relaxation oscillations of accretion discs in which cool hydrogen ionization regions provide a triggering mechanism. As a guide for understanding the global instabilities, an associated local analysis was carried out and a fundamental role in this was played by the fact that when the values of the accretion rate, \dot{M} , and the surface density, Σ , at a particular location (value of r) are plotted against each other for a sequence of equilibrium models, the points form characteristic S-shaped curves in the $\log \dot{M} - \log \Sigma$ plane. Analogous investigations of the time-dependent evolution of accretion discs around neutron stars and black holes were started by Taam and Lin (1984) who found that if the viscous stress tensor is proportional to the total pressure, global analysis confirms the results inferred from local analysis and the instability manifests itself in terms of short time-scale luminosity fluctuations. Similar studies were performed subsequently by Lasota and Pelat (1991) and more recently by Chen and Taam (1994). Lasota and Pelat concluded that the (locally) thermally unstable region in the inner part of the disc always becomes effectively optically thin and that the evolution and disc structure depends sensitively on the treatment of the transitions between the optically thick and optically thin regimes. Chen and Taam (1994) investigated the global evolution of thermal-viscous instabilities in the case where the viscous stress is proportional to the gas pressure with a particular form for the viscosity parameter. Their calculations show that the instabilities are globally coherent throughout the entire unstable region of the disc.

All of the authors mentioned above studied Keplerian discs. The only investigation which we know of in which a full set of time-dependent equations has been solved, is the one by Honma, Matsumoto and Kato (1991).

The importance for accretion discs around black holes of the transonic nature of the flow, deviations from Keplerian rotation and non-local cooling by advection, was first pointed out by Paczyński and Bisnovatyi-Kogan (1981) who constructed

a simple global equilibrium model of a geometrically thin steady disc. A full treatment, including all of these effects, was formulated by Loska (1982) and Muchotrzeb and Paczyński (1982). Following their approach, Abramowicz, Czerny, Lasota and Szuszkiewicz (1988) calculated a sequence of slim accretion disc models for a wide range of accretion rates and found S-shaped curves in $\log \dot{M} - \log \Sigma$ plane, a result which was later confirmed by Abramowicz, Kato and Matsumoto (1989). This finding recalls the situation for dwarf novae (although the physical processes leading to this shape are quite different in the two cases) and this encouraged Honma, Matsumoto and Kato (1991) to study the nonlinear evolution of the thermally unstable models to see whether similar behaviour occurred. They found that, at least for high viscosities ($\alpha = 0.1$), a limit-cycle behaviour does indeed occur which is very reminiscent of that for dwarf novae.

The aim of our present study was to examine the global behaviour of the thermally unstable slim disc models in their original formulation (Abramowicz, Czerny, Lasota and Szuszkiewicz, 1988) with low viscosity ($\alpha = 0.001$). The effects of advective cooling are included and our results represent a suitable standard reference for making comparison with results from forthcoming calculations in which further non-local processes will be included which were not present in the original version of the slim disc model.

In Section 2, we discuss the set of basic equations used for our calculations, pointing out which assumptions are made and describing the averaging procedure employed. The numerical treatment of the equations is presented in Section 3. In Section 4 the global behaviour of the models is shown and in Section 5 the same models are viewed locally. Section 6 contains comments and conclusions.

2 Basic equations

In this section, we present the equations used for calculating non-stationary behaviour of the original slim disc model and highlight the assumptions involved in this treatment.

2.1 Evolution equations

We consider here an axisymmetric non-self-gravitating fluid disc formed in the gravitational potential Φ of a black hole with mass M and use cylindrical polar coordinates (r, φ, z) centred on the black hole. The symmetry axis, z , coincides with the rotation axis of the disc. The behaviour of the fluid is governed by the basic hydrodynamical equations for conservation of mass, energy and momentum (radial, angular and vertical). We study a one-dimensional formulation in which most of the equations are written in a vertically integrated form with the vertical structure being approximated under the assumptions that hydrostatic balance always holds in the vertical direction and that flow properties above and below the equator ($z = 0$) are the same. In this picture, the velocity field is approximated by $v_z = 0$, $v_r = v_r(r, t)$ and $v_\varphi = v_\varphi(r, t)$. Newtonian mechanics is used and general relativistic effects, which become significant near to the inner edge of the disc, are simulated by using the pseudo-Newtonian potential introduced by Paczyński and Wiita (1980):

$$\Phi = -\frac{GM}{\sqrt{r^2 + z^2} - r_G}. \quad (1)$$

Here r_G is the Schwarzschild radius defined by $r_G = 2GM/c^2$, where G and c are the gravitational constant and velocity of light respectively.

Within this framework, the evolution equations can be written in the following form:

– *Mass conservation equation:*

$$\frac{D\Sigma}{Dt} = -\frac{\Sigma}{r} \frac{\partial}{\partial r} (rv_r) \quad (2)$$

where D/Dt is the Lagrangian derivative given by

$$\frac{D}{Dt} = \frac{\partial}{\partial t} + v_r \frac{\partial}{\partial r},$$

$\Sigma = \Sigma(r, t)$ is the surface density obtained by vertically integrating the volume density ρ

$$\Sigma = 2 \int_0^H \rho dz \quad (3)$$

with H being the half-thickness of the disc, and $v_r = Dr/Dt$ (which is negative for an inflow). For the stationary case, the mass conservation equation reduces to the statement that the local accretion rate is the same at all locations in the disc

$$\dot{m}(r) = -2\pi r \Sigma v_r = \dot{M}, \quad (4)$$

where $m(r)$ is the total mass internal to the cylindrical radius r , $\dot{m} = \partial m/\partial t$ and \dot{M} is the rate of increase of mass of the black hole.

– *Radial equation of motion:*

$$\frac{Dv_r}{Dt} = -\frac{1}{\rho} \frac{\partial p}{\partial r} + \frac{(l^2 - l_K^2)}{r^3} + F_{rr} - F_{\varphi\varphi}, \quad (5)$$

where p is the pressure, $l = l(r, t) = rv_\varphi(r, t)$ is the specific angular momentum, l_K is the value of l for Keplerian motion with $v_\varphi = [-r(d\Phi/dr)]^{1/2} = [GMr/(r - r_G)^2]^{1/2}$. F_{rr} and $F_{\varphi\varphi}$ are the viscous forces:

$$F_{rr} = \frac{1}{r\rho} \frac{\partial}{\partial r} (r\tau_{rr})$$

$$F_{\varphi\varphi} = \frac{1}{r\rho} (\tau_{\varphi\varphi})$$

where

$$\tau_{rr} = \frac{2}{3}\mu \left[2\frac{\partial v_r}{\partial r} - \frac{v_r}{r} \right]$$

$$\tau_{\varphi\varphi} = \frac{2}{3}\mu \left[\frac{2v_r}{r} - \frac{\partial v_r}{\partial r} \right]$$

and μ is the shear viscosity coefficient (bulk and radiative viscosities are not considered anywhere in the present treatment). The importance of the viscous forces F_{rr} and $F_{\varphi\varphi}$ has been pointed out (e.g. by Papaloizou and Stanley, 1986) and they have been considered in the more recent studies but we do not include them here since they were not part of the original slim disc model. Also, in accordance with the original slim disc model, we do not vertically integrate the radial equation of motion but, instead, solve it in the equatorial plane. We comment further on this in Section 2.2.

The stationary version of Eq. (5) is

$$v_r \frac{dv_r}{dr} = -\frac{1}{\rho} \frac{dp}{dr} + \frac{(l^2 - l_K^2)}{r^3} \quad (6)$$

– *Azimuthal equation of motion, for the specific angular momentum, l :*

$$\frac{Dl}{Dt} = \frac{1}{r\Sigma} \frac{\partial}{\partial r} \left(r^2 2 \int_0^H \tau_{\varphi r} dz \right) \quad (7)$$

where the rate of shearing is

$$\tau_{\varphi r} = \mu r \frac{\partial \Omega}{\partial r} \quad (8)$$

which, following Shakura and Sunyaev (1973), is often approximated by

$$\tau_{\varphi r} = -\alpha p \quad (9)$$

where α is a (constant) viscosity parameter. This form, which can be derived from Eq. (8) in the case of a (stationary) Newtonian Keplerian disc and with the aid of several additional approximations, is the one used in the present paper in accordance with the original slim disc model. However, a major objective of our future work concerns investigation of the extent to which inclusion of a more physical viscosity prescription causes differences in non-stationary behaviour with respect to that of the “standard” models calculated here. With expression (9), Eq. (7) can be rewritten as

$$\frac{Dl}{Dt} = -\frac{\alpha}{r\Sigma} \frac{\partial}{\partial r} (r^2 P) \quad (10)$$

where P is the vertically-integrated pressure

$$P = 2 \int_0^H p dz \quad (11)$$

For a stationary model, Eq. (10) can be integrated explicitly and, using the boundary condition that there is no viscous torque at the black hole horizon, this gives

$$\dot{M}(l - l_0) = 2\pi\alpha P r^2 \quad (12)$$

where l_0 is the specific angular momentum at the inner edge of the disc.

– *Vertical equation of motion:*

$$\frac{Dv_z}{Dt} = -\frac{1}{\rho} \frac{\partial p}{\partial z} - \frac{\partial \Phi}{\partial z} + F_{zz}, \quad (13)$$

where the the viscous force F_{zz} is given by

$$F_{zz} = \frac{1}{\rho} \frac{\partial}{\partial z} \tau_{zz}$$

with

$$\tau_{zz} = -\frac{2\mu}{3r} \frac{\partial}{\partial r} (rv_r).$$

However, F_{zz} is not included in the present treatment. Also, since we are considering hydrostatic equilibrium in the vertical direction, the acceleration term vanishes. We note that neglecting the vertical acceleration may be a rather poor approximation in some parts of the disc, as suggested by two-dimensional studies (Papaloizou and Szuszkiewicz, 1994), and investigation of the effect of *not* neglecting it is one of the important issues to be addressed in our forthcoming study. The approach used here is exactly the same as for the stationary slim disc models and is discussed further in Section 2.2.

– *Conservation of thermal energy:*

$$\rho T \frac{DS}{Dt} = Q_{vis} + Q_{rad}, \quad (14)$$

where S is the entropy per unit mass, T is the temperature, Q_{vis} is the rate at which heat is generated by viscous friction (including the effects of stresses in both the azimuthal and radial directions)

$$Q_{vis} = \frac{4}{3}\mu \left[\left(\frac{\partial v_r}{\partial r} \right)^2 + \left(\frac{v_r}{r} \right)^2 - \frac{v_r}{r} \frac{\partial v_r}{\partial r} \right] + \mu \left(r \frac{\partial \Omega}{\partial r} \right)^2, \quad (15)$$

and Q_{rad} is the rate at which heat is lost or gained by means of radiative energy transfer (expressed as the sum of terms for the radial and vertical directions)

$$Q_{rad} = \frac{1}{r} \frac{\partial}{\partial r} \left[\chi_r r \frac{\partial T}{\partial r} \right] + \frac{\partial}{\partial z} \left[\chi_r \frac{\partial T}{\partial z} \right] \quad (16)$$

where $\chi_r = 4acT^3/3\kappa\rho$ is the radiative conductivity, a is the radiation constant and κ is the opacity. In the present treatment, the first terms on the right hand side of Eqs. (15) and (16) are omitted. Thermal conductivity is not considered here. Using the strategy discussed in Section 2.2, the vertically-integrated form of Eq. (14) can be written in the following way

$$\frac{DT}{Dt} = \frac{\alpha r T (\partial \Omega / \partial r)}{0.67(12 - 10.5\beta)} - \frac{TF^-}{0.67pH(12 - 10.5\beta)} + \frac{(4 - 3\beta)}{(12 - 10.5\beta)} \frac{T D\rho}{\rho Dt} \quad (17)$$

where p , ρ and T are the values of these quantities on the equatorial plane, β is the ratio of the gas pressure to the total pressure and F^- is the radiative flux away from the disc in the vertical direction for which we use the expression

$$F^- = \frac{12acT^4}{3\kappa\rho H},$$

as discussed in Section 2.2. The stationary form of Eq. (17) is

$$\dot{M}(l - l_0)\left(-\frac{d\Omega}{dr}\right) + 0.67\dot{M}T\frac{dS}{dr} = 4\pi r F^-. \quad (18)$$

The thermodynamic quantities in the equatorial plane are taken to obey the equation of state

$$p = k\rho T + \frac{a}{3}T^4 \quad (19)$$

and the opacity is approximated by the Kramers formula for chemical abundances corresponding to those of Population I stars

$$\kappa = 0.34 \times (1 + 6 \times 10^{24} \rho T^{-3.5}). \quad (20)$$

Use of this formula represents the only genuine difference between the original slim disc formulation and its time-dependent version considered here. The original slim disc model used the opacities of Cox and Stewart (1970) stored in the form of a table. We have checked that stationary models calculated with these two different opacity treatments do not differ significantly from each other.

2.2 Treatment of the vertical structure

If the disc is not geometrically thick, it is possible to work in terms of vertically-integrated variables and to solve an essentially one-dimensional problem. However, passing from standard to vertically-integrated variables cannot be done rigorously as the vertical structure of the disc is not known in detail. Several approximate procedures have been introduced for dealing with this. We describe here the approach followed in the present treatment and make comparison with the alternative approach of Honma, Matsumoto and Kato (1991) (hereafter referred to as HMK).

Neglecting the zz -viscous stress tensor component and the vertical acceleration term, Eq. (13) becomes the standard equation of hydrostatic equilibrium:

$$\frac{\partial p}{\partial z} = -\rho \frac{\partial \Phi}{\partial z}. \quad (21)$$

If one makes the assumption that p and ρ can be linked (in the vertical direction) by the polytropic relation $p \propto \rho^{1+1/N}$, where N is the polytropic index, Eq. (21) can be directly integrated (Hoshi, 1977) to give

$$\Omega_K^2 H^2 = 2(1 + N) \frac{p_0}{\rho_0}, \quad (22)$$

$$\rho(z) = \rho_0 \left(1 - \frac{z^2}{H^2} \right)^N, \quad (23)$$

where the subscript 0 denotes equatorial plane quantities and Ω_K is the Keplerian angular velocity given by $\Omega_K = [GM/r(r - r_G)^2]^{1/2}$. (Hoshi used the Newtonian gravitational potential rather than the pseudo-Newtonian one but Eqs. (22) and (23) are the same in either case.) HMK used $N = 3$ for their vertical integrations and in this case, $\Omega_K^2 H^2 = 8p_0/\rho_0$ but we follow Paczyński and Bisnovatyi-Kogan (1981) and use

$$\Omega_K^2 H^2 = 6 \frac{p_0}{\rho_0}, \quad (24)$$

as our equation for H .

In order to calculate the surface density Σ , the expression (23) can be inserted into Eq. (3) and the integral performed directly. For $N = 3$ one obtains $\Sigma = (32/35)\rho_0 H$ and this was the expression used by HMK. A very similar result is obtained if ρ is taken to be a linear function of z with $\rho(0) = \rho_0$ and $\rho(H) = 0$. In this case $\Sigma = \rho_0 H$. If, instead, one took the density to be *constant* in the vertical direction, with $\rho(z) = \rho_0$, then the result would be $\Sigma = 2\rho_0 H$ which is rather different. The difference between the first two expressions is small and, given the approximation introduced when using the polytropic law, there is no particular reason to prefer one over the other. We use

$$\Sigma = \rho_0 H, \quad (25)$$

for conformity with earlier work. A similar discussion applies for the vertically integrated pressure P , for which we use

$$P = p_0 H. \quad (26)$$

For the radial equation of motion, we use Eq. (5) with the quantities involved taking their equatorial-plane values. HMK, on the other hand, used the vertically-integrated form

$$\frac{Dv_r}{Dt} = -\frac{1}{\Sigma} \frac{\partial P}{\partial r} + \frac{(l^2 - l_K^2)}{r^3} - \frac{P}{\Sigma} \frac{d \ln \Omega_K}{dr}, \quad (27)$$

which contains the new term $(P/\Sigma)(d \ln \Omega_K / dr)$ coming from the vertical integration of the gravitational potential. The question of the importance of this term for time-

dependent calculations has been investigated by Chen (private communication) who concludes that it does not make any significant difference.

The thermodynamic relation for the entropy used in our version of the thermal energy conservation equation is calculated for a mixture of black body radiation and a simple perfect gas with the polytropic index, N , being set equal to $3/2$. This gives

$$T \frac{DS}{Dt} = \frac{p}{\rho} \left[(12 - 10.5\beta) \frac{1}{T} \frac{DT}{Dt} - (4 - 3\beta) \frac{1}{\rho} \frac{D\rho}{Dt} \right]. \quad (28)$$

HMK used the rather similar expression

$$\rho T \frac{DS}{Dt} = \frac{1}{\Gamma_3 - 1} \left[\frac{Dp}{Dt} - \Gamma_1 \frac{p}{\rho} \frac{D\rho}{Dt} \right] \quad (29)$$

which is derived for $c_V = \text{constant}$ (c_V being the specific heat at constant volume). Here Γ_1 and Γ_3 are the generalized adiabatic indices. In their integration procedure, they used the fact that for $N = 3$, β does not depend on z . The HMK expression for the radiative flux F^- (in the integrated energy equation) is

$$F^- = \frac{16acT^4}{3\kappa\rho H}$$

which differs from ours by a numerical factor. Comparison between the stationary solutions obtained by Szuszkiewicz (1988) and those obtained by HMK shows that the results depend only very weakly (if at all) on the procedure used for the vertical integration (Abramowicz, Kato and Matsumoto, 1989). It is not necessarily the case, however, that the same will hold for time-dependent calculations. Indeed, Shakura and Sunyaev (1976) pointed out that numerical estimates for instability growth rates and characteristic wavelengths can be sensitive to the procedure adopted for approximating the vertical structure.

3 The method used for solving the equations numerically

3.1 The Lagrangian evolutionary code

The equations presented in Section 2 have been solved numerically, using a Lagrangian finite difference scheme with standard Lagrangian differencing and grid organization. The code was adapted from one developed by Miller and Pantano (1990) in a different context. The integration domain extended from a suitable position in the supersonic part of the flow (for most of the models presented here, this was set at $r \approx 2.5 r_G$) out to several thousand r_G and was divided into a succession of comoving annular zones with each one containing a mass 12% larger than the one interior to it. The mass of the innermost zone was determined in accordance with

numerical convenience. The mass, m , interior to a given zone boundary was used as the radially-comoving independent variable, following the usual practice for Lagrangian calculations, and the equations of Section 2.1 were rewritten accordingly, with radial gradients being transformed using

$$\frac{\partial}{\partial r} = 2\pi r \Sigma \frac{\partial}{\partial m}.$$

During the progress of each calculation, a regridding was carried out every time that the inner edge of the innermost zone crossed $2.5 r_G$ in the course of being accreted. The innermost zone was then removed from the calculation and all of the variables were interpolated onto a new grid having a similar structure (in terms of intervals in the independent variable m) to that at the initial time. The interpolation (which requires great care in order to avoid introducing destructive inaccuracies) was carried out using a piecewise cubic method. With the grid organization which we use, adequate spatial resolution is normally obtained with 200 - 300 zones (except in the special cases mentioned earlier) and the runs have extended for as many as $10^8 - 10^9$ timesteps. The increase in mass of the black hole during the calculations, due to accretion of material from the disc, was extremely small (always less than one part in 10^{10} for the models studied here).

The equations are solved for v_r , r , Σ , T and l as the main dependent variables. (From this point onwards, the thermodynamic parameters p , ρ and T will always be taken to refer to values on the equatorial plane.) Our numerical scheme has roughly second-order accuracy in space and in time, the latter being achieved with the use of intermediate time-levels in a standard way. Σ and T are treated as zone-centre quantities and computed at the full time-level; r is taken as a zone-boundary quantity, computed at the full time-level and v_r and l are taken as zone-boundary quantities, computed at the intermediate time-level. The time-step is adjusted in accordance with the Courant condition and with two additional constraints on the fractional variations of ρ and T in any single time-step.

The continuity equation (2) is rewritten in a form which is more convenient for the numerical calculations:

$$\frac{D}{Dt} (A_{i-1/2} \Sigma_{i-1/2}) = 0, \quad (30)$$

where i is the index of zone boundaries, with $i - 1/2$ referring to a mid-zone, and $A_{i-1/2}$ is the zone area given by

$$A_{i-1/2} = \pi(r_i^2 - r_{i-1}^2).$$

The energy equation (17) is solved implicitly for T by means of an iterative procedure, using the secant method. Extrapolation of previous time-step values is used to provide initial estimates, and convergence to machine accuracy is typically achieved with 4 or 5 iterations. In the viscous heating term, the gradient of the angular velocity is substituted by the gradient of the *Keplerian* angular velocity, an approximation which had been used previously in the stationary calculations in order to avoid a serious numerical instability which otherwise occurred there (Muchotrzeb

and Paczyński, 1982). In the present time-dependent calculations, we followed the same line in order to remain as close as possible to the original slim disc approach.

When values are known for r , Σ and T , p , ρ and H can then be found by solving simultaneously the integrated equation of vertical hydrostatic equilibrium (24), the solution of the integral for Σ (25) and the equation of state (19). These equations are manipulated algebraically to yield a quadratic equation for ρ which is then solved analytically. The solution for p , ρ and H is embedded in the iteration loop for T . We take this occasion to emphasize that it is necessary to maintain very high levels of accuracy throughout the various stages of these calculations as there is a very close balance of terms in both the energy equation and the radial equation of motion.

A simple form of numerical diffusion is introduced when solving the radial equation of motion (5) for v_r . In the finite difference representation of this equation, $(v_r)_i^n$ ($(v_r)_i$ evaluated at the old time level t^n) is substituted by

$$\left[k(v_r)_{i-1}^n + (1 - 2k)(v_r)_i^n + k(v_r)_{i+1}^n \right] \quad (31)$$

with the value $k = 10^{-3}$ being selected on the basis of numerical experiments. The reason for introducing this modification of the standard scheme will be explained in Section 6.

The inner edge of the grid was placed well within the supersonic part of the flow, so that the inner boundary conditions could not affect the evolution external to the sonic point. For sub-Eddington stationary models, the sonic radius is near to that of the marginally stable orbit at $r = 3r_G$ and so $r = 2.5r_G$ is suitable as an initial location for the inner edge of the grid. During the subsequent evolution, a check is kept to make sure that the sonic point never gets too close to the grid boundary. At every time step, it is necessary to set boundary conditions for v_r and l at both the inner and outer edges of the grid. At the inner edge, l is set equal to its value at the next grid point, which is a very good approximation since the specific angular momentum is very nearly constant in this region, while v_r is calculated from the standard equation (5) with the pressure gradient set to zero (which is also an excellent approximation). The outer edge of the grid is set at several thousand r_G where there is essentially no change in the variables during the time of the calculation and so l and v_r are kept constant there.

3.2 Initial conditions and perturbations

As initial conditions for the evolutionary calculations, we used the stationary transonic disc models constructed by Szuszkiewicz (1988) and described by Abramowicz, Czerny, Lasota and Szuszkiewicz (1988). The parameters characterizing these models are: the mass of the black hole M , the accretion rate \dot{M} which we measure in units of the critical value $\dot{M}_c = 64\pi GM/c\kappa$ (the accretion rate for which the luminosity is equal to L_E), and the viscosity parameter, α . For models with accretion rates up to the critical one, \dot{M}/\dot{M}_c is equal to the luminosity of the disc measured in units of the Eddington luminosity, $L_E = 4\pi GMm_p c/\sigma_T \approx 10^{38}(M/M_\odot)$, erg/s where m_p is the proton mass and σ_T is the Thomson cross section for electron scattering. We will use \dot{M}/\dot{M}_c and L/L_E interchangeably for the sub-Eddington and Eddington models which are the main focus of our present investigation. All of the

models discussed here have the same M and α ($M = 10M_\odot$ and $\alpha = 10^{-3}$) but \dot{M}/\dot{M}_c varies over a wide range of values.

For starting the time-dependent calculations, the initial data from the appropriate stationary model is first read in from a file and transferred onto the finite-difference grid. This is a very delicate procedure since, as mentioned earlier, there is a close balance between large terms both in the radial equation of motion and in the energy equation. The former is particularly sensitive. It is important to transfer the minimum possible number of variables onto the grid and then to calculate other quantities from the representations of these basic ones on the grid. If this is not done, inconsistencies arise which destroy the calculation. Despite the fact that the evolutionary code uses five dependent variables (r , v_r , Σ , T and l), it is only necessary to transfer the first four of these from the stationary model since l can then be calculated from Eq. (5) on the grid bearing in mind that, for a stationary model, $Dv_r/Dt = v_r dv_r/dr$. Proceeding in this way turned out to be crucial for the success of the calculation.

The process of transferring the initial data onto the finite difference grid together with the action of numerical noise which inevitably enters during the calculation, turn out to be sufficient for introducing suitable generalised perturbations into the model to trigger growth of unstable modes which may be present. A lower limit on the wavelength of perturbations is, of course, set by the grid spacing but this is amply fine enough to include the wavelengths of interest.

4 Global behaviour of the models

We have found three different types of global behaviour for the present initially stationary slim disc models depending on the accretion rate or, equivalently, on the luminosity. Models with $L \leq 0.08 L_E$ are stable. Models with L between 0.09 and $1 L_E$ develop a violently unstable shock-like feature near to the sonic point, which is thought to lead to disruption of the disc, and our calculation then terminates. Finally, models with super-Eddington luminosities show progressive slow evolution. We concentrate here on the sub-Eddington models, leaving discussion of the super-Eddington ones for a forthcoming paper.

As background for our discussion of the results of the time-dependent calculations, it is useful to review briefly the predictions of local stability analysis carried out for stationary models. The simplest local stability criterion states that if, at a certain radius, the ratio of gas pressure to total pressure, β , is smaller than 0.4, then the disc will be unstable at that radius. We have constructed a sequence of stationary models, with a range of luminosities, and key parameters are listed in Table 1. The local stability criterion has been applied at every radius for each model and the locations of predicted unstable regions have been determined. If, instead, we use the refined criterion derived by Pringle (1976), the predicted unstable regions remain essentially the same for all of the models except the one with $L = 0.07 L_E$ for which the range becomes $6.2 - 9.0 r_G$. This small difference is due to Pringle's result that when electron scattering does not provide the dominant opacity, the disc is thermally stable even when the dominant contribution to the pressure comes from radiation. The models with luminosity less than $0.07 L_E$ are predicted to be stable on the basis of local analysis. For $L \geq 0.07 L_E$, the disc can be divided into three regions: an inner locally stable zone extending from the sonic point (at r_{sonic}) out to the inner edge of the unstable region, the unstable zone (the location of which is

given in Table 1) and finally an outer stable zone.

Following Shakura and Sunyaev (1976), it is possible to give a more extended description of the stability properties of our stationary models, still on the basis of local linear analysis. While this description is somewhat incomplete and has limitations, it is nevertheless quite instructive. For each model, we evaluate the bifurcation wavelength, which we will call Λ_{min} . Perturbations with wavelengths, Λ , satisfying $2H < \Lambda < \Lambda_{min}$ give concentric waves travelling across the surface of the disc while for $\Lambda \geq \Lambda_{min}$ there are two branches of growing modes which take the form of standing waves. For the first of these branches, the perturbation growth rate decreases with increasing wavelength and in the limit $\Lambda \gg H$ this becomes the instability discovered by Lightman and Eardley (1974). On the second branch, the growth rate *increases* with increasing wavelength and growth of these modes is due to the thermal instability found by Pringle, Rees and Pacholczyk (1973). The characteristic growth time, given by Shakura and Sunyaev, is

$$\tau = \frac{56 - 45\beta - 3\beta^2}{30(0.4 - \beta)} t_{th}, \quad (32)$$

with the thermal time scale t_{th} being given by

$$t_{th} = \frac{1}{\alpha\Omega}.$$

The growth time, τ , is different for different radii. In Table 1 we give its minimum value for each model, τ_{min} , and the location in the disc where this minimum is attained, $r(\tau_{min})$. Each of the stationary models listed was evolved forward in time with our time-dependent code, as described earlier, and the final column of the table shows the (physical) time for which each of these calculations was continued. This represents either the time at which the calculation was discontinued because of catastrophic instability growth or the time beyond which it was no longer considered to be of interest to continue.

The aim of our time-dependent calculations was to determine which models are *globally* unstable and to see how the instabilities evolve with time. Firstly, as a test of the code, we calculated the evolution of the model with $L = 0.01 L_E$ which is *stable* according to the linear analysis. Without modification, the original basic code showed even this model becoming unstable but we found that the instability could be removed by introducing a very small amount of additional numerical diffusion into the scheme, following the prescription of Eq. (31). The additional diffusion was then retained for all of the models studied. We will discuss this further in Section 6.

Models with $L = 0.07$ and $0.08 L_E$ were not found to develop any global instability, a result which could already be explained within the context of the local analysis since the minimum wavelength Λ_{min} , necessary for the onset of the thermal instability, is larger than the width of the unstable region for these models.

For L in the range from 0.09 to $1 L_E$, the evolution is terminated by the formation of a narrow velocity spike adjacent to the sonic point which, once initiated, grows very rapidly in amplitude and disrupts the solution. As a representative example of these cases, the global behaviour of the model with $L = 0.1 L_E$ is illustrated in Figures 1, 2, 3 and 4 which show the radial profiles of the radial velocity divided

by the sound speed (i.e. the Mach number), the surface density, the temperature and the thickness of the disc, at several time-levels during the evolution. An initial instability begins to grow gradually in the region predicted to be unstable by the local linear analysis and the influence of this then spreads inwards to the sonic point, where it triggers a second, more violent, instability (as shown in Figure 5). This is a fundamentally non-local process. For this particular model, the perturbation in v_r/c_s associated with the initial instability extends outwards to beyond $10 r_G$ and, by the time that the run is ended, it has saturated in amplitude and a small region of positive (outward) radial velocity has appeared, peaking at $\sim 7 r_G$. There are corresponding variations in the other parameters, which are in the sense of increasing temperature and disc thickness and decreasing surface density in the region of the initial instability. The sonic point moves progressively inwards (despite what might be inferred from Figure 1). As will be seen from the local views of the global behaviour presented in Section 5, the local accretion rate at around $3 r_G$ increases more quickly than that at $5 r_G$ and this leads to an emptying of the inner part of the disc. For $L = 0.1 L_E$, the velocity spike near to the sonic point starts to appear almost simultaneously with the saturation in amplitude of the initial perturbations in v_r/c_s and T and, once initiated, the growth occurs very rapidly (in $\sim 7 \times 10^{-3}$ s, i.e. on the dynamical timescale) with a shock-like structure developing at the leading edge of the spike. There are corresponding rapid changes in the profiles of the other variables. The growth of this feature appears to be catastrophic and, certainly, we are not able to continue the evolution further with our present numerical scheme. However, we are not able to completely rule out the possibility that there might be a stabilization in the non-linear regime which could be followed with a more sophisticated numerical treatment. We have checked, a posteriori, that even under these most extreme conditions the models remain optically thick, according to the criterion $(\kappa_e \kappa_{ff})^{1/2} (\Sigma/2) > 1$, both in the expanded innermost part and in the region of the velocity spike. Since we strongly suspect that the velocity spike will be suppressed or severely altered as a result of including improvements to the original slim disc model, we delay further consideration of its origin and behaviour until a subsequent paper where the effects of such improvements will be systematically discussed.

While the case $L = 0.1 L_E$, discussed in detail above, is largely representative of the others with L in the range from 0.09 to $1 L_E$, there is a difference appearing for models with slightly higher luminosity which needs to be mentioned here. With the case just considered, the run is halted by the growth of the velocity spike almost immediately the saturation occurs in the initial perturbation. However, it can be seen (particularly in Fig. 2 for T) that the feature associated with the initial instability is then just starting to propagate outwards. In higher luminosity models, such as the one with $L = 0.2 L_E$ which we will discuss in the next section, this feature has time to propagate outwards significantly before the run is ended. It is tempting to speculate that this might, perhaps, have been the beginning of a cyclic behaviour if the instability near to the sonic point had not intervened.

5 Local view of the global behaviour - S-curves and evolutionary tracks

The existence of S-curves in the $\log \dot{M} - \log \Sigma$ plane for sequences of models of stationary accretion discs around black holes, provided a motivation to look for nonlinear cyclical behaviour in these systems in analogy with the situation for dwarf

novae. The local stability of a disc at a given radius, r , is related to the location of the model on the S-curve for that radius. The lower and middle branches of the S-curve correspond to the standard Shakura/Sunyaev models and are simply loci representing the balance between viscous heating and radiative cooling. Discs on the lower branch are thermally stable while those on the middle branch are unstable and a transition via marginal stability occurs at the lower turning point. The upper branch has a positive slope which might indicate stability, but here the situation is different from that for dwarf novae. On the upper branch here, the heat generated by viscosity is mainly advected with the accretion flow, rather than being mainly radiated away as on the lower branches, and standard local analysis is not adequate for determining whether these models are stable or not.

Having made our global calculations as described in the previous section, we can then take a local view of them, considering the time variation of parameters at a particular fixed location r . Following earlier work on local analysis of stationary models, it is convenient to consider plots of $\log \dot{m}$ against $\log \Sigma$ but it should be noted that the trajectories exit from these plots whenever there is a local outflow, $\dot{m} < 0$. For the case shown in Fig. 1 ($L = 0.1 L_E$), the local outflow is seen only at the very end of the run but for models with higher luminosity, the outflow feature can sometimes be seen passing by the monitoring location. In Figure 6, we show the trajectory of parameters at $r = 8 r_G$ for a model with $L = 0.2 L_E$. (Here and in the rest of this section, \dot{m} is measured in units of the critical accretion rate, \dot{M}_c .) The dashed lines mark rapid motion out of (or into) the parameter space, corresponding to \dot{m} changing sign. In this case, \dot{m} remained negative for 14 seconds before becoming positive again.

This figure is the first of a sequence of similar ones showing different models and monitoring locations and so we take this opportunity to describe the way in which all of them should be viewed. Stationary models covering the whole range of luminosities are located along the S-shaped curve shown by the dotted line and we plot the phase-space trajectory for the particular model of interest at the selected monitoring location together with corresponding trajectories for a set of comparison models having initial $\dot{m} = 0.01, 0.07, 0.08, 1$ and 10 . We recall that for the initial stationary models, $\dot{m}(r) = \dot{M} = \text{const}$ and \dot{m} measured in units of \dot{M}_c is equal to L/L_E for those models which are not super-Eddington. Identification of the different initial models is straightforward as it is sufficient to look at the corresponding value of \dot{m} on the axis. For each model, the open square shows the initial state and the filled square shows the state at the end of the calculation with the line joining them indicating the phase space trajectory followed. Models for which it is not possible to see any change in location on the scale of this plot have the filled square superimposed on the open one so that only the filled square is seen. Models with initial $\dot{m} = 0.01, 0.07$ and 0.08 are globally stable and always remain at essentially the same point in the phase space for the given radius. The model with Eddington luminosity, $\dot{m} = 1$, evolved for only a very short time before the run terminated and so it is only for small radii (where the evolutionary time-scale is shorter) that any movement can be seen in the phase space. Finally the super-Eddington model, which we are not discussing in detail here, shows similar sorts of trajectory at the different radii.

Although local analysis for discs around neutron stars and black holes is normally discussed in terms of the $\dot{m} - \Sigma$ relation, most authors presenting results from time-dependent calculations have shown local views in the $\log T - \log \Sigma$ plane instead of the $\log \dot{m} - \log \Sigma$ one. This is reasonable since T and Σ are primary quantities calculated in the numerical codes, whereas \dot{m} is a secondary quantity used just for interpretation, and also there is the problem mentioned earlier, that negative values

of \dot{m} cannot be represented in a plot of $\log \dot{m}$ against $\log \Sigma$. In Figure 7 (which focuses on our “standard” model with $\dot{m} = 0.1$) we show trajectories in both planes for comparison. Four different monitoring locations are used (at 3, 5, 8 and $10 r_G$) and the frames are arranged in two columns, one for $\log \dot{m} - \log \Sigma$ and the other for $\log T - \log \Sigma$. The general conclusions which can be drawn from considering the qualitative differences between the evolutionary tracks for different radii, are that different parts of the disc do not react in a synchronized way and that the instability behaviour seen has a global character. Our discussion will mainly be related to the $\log \dot{m} - \log \Sigma$ curves.

For $r = 3 r_G$, viewed in terms of $\log \dot{m} - \log \Sigma$, the model evolves along the lower branch of the S-curve for 178 s but then overshoots the position where the S-curve bends and makes an attempt to come back again. However, soon after it turns and changes its direction, it starts to follow a quite dramatic path and the run is halted soon after this. We know, from the global behaviour, that this is caused by the development of the instability at the sonic point. The evolutionary track in the $\log T - \log \Sigma$ plane is less dramatic, but it is clear also from this that the evolution is not going to follow any closed path as would be necessary for having a limit cycle behaviour. The situation at $5 r_G$, if viewed in isolation, would have seemed promising for producing a limit cycle behaviour, especially looking at the $\log T - \log \Sigma$ plane where the model follows a well-behaved regular path, but it is important to notice that the local accretion rate here grows significantly less than that at $3 r_G$ giving rise to an unbalanced situation producing a drop in surface density. The local accretion rates at 8 and $10 r_G$ decrease in time, making the effect even more pronounced. This description complements the global view of the behaviour of the surface density shown in Figure 3.

For models with higher accretion rates, the importance of the transonic nature of the flow, deviation away from Keplerian rotation and advective cooling becomes progressively greater. To investigate how these non-local effects influence the evolution of models with higher accretion rates, we made calculations for several models with luminosities between 0.1 and $1 L_E$. In Figure 8, we show the evolutionary paths for $L = 0.2, 0.4$ and $0.8 L_E$ at 3 and $5 r_G$. The evolution for $L = 0.2 L_E$ (which we have already discussed in connection with Fig. 6, drawn for $8 r_G$) proceeds in a rather similar way to that for $0.1 L_E$ except that the velocity perturbation is here able to propagate outwards significantly and the run terminates with unstable behaviour at the sonic point after a shorter time (71 s in this case). These features might seem contradictory at first sight but it should be noted that the radial velocities are higher for $0.2 L_E$ and so everything proceeds more rapidly. Moving to models with higher luminosities, already for $L = 0.4 L_E$ the situation becomes significantly different. Now, the local accretion rate increases systematically at *all* of the radii considered in Fig. 7. The Mach number perturbation propagates out to around $25 r_G$ but never gives any local outflow. For $L = 0.8 L_E$ the Mach number perturbation does not have enough time to propagate outwards before the unstable behaviour at the sonic point terminates the run (after 25 s). This is directly connected with the fact that the drift time $t_{dr} = r/v_r$ (which becomes progressively shorter for models with higher accretion rates) is now comparable with the thermal time-scale (Szuszkiewicz, 1990). By this stage, it is no longer the case that the thermal instability determines the evolution of the disc.

Our results indicate that the models presented here with luminosities in the range 0.09 - $1 L_E$ are globally unstable and that the demarcation line between globally stable and globally unstable models lies between 0.08 and $0.09 L_E$. It is interesting to compare the trajectories in the $\log T - \log \Sigma$ plane for models on either side of the demarcation line. Figure 9(a) shows trajectories for two models above it: 0.09

and $0.1 L_E$, at $r = 8 r_G$. We focus attention on the one with $0.09 L_E$ (which is nearer to the demarcation line) and note the evolution starting along an unwinding spiral and then diverging off towards higher temperatures. From the corresponding time series for the temperature variations, shown in Figure 9(b), we see the temperature starting to oscillate with growing amplitude but then quickly turning to unbounded growth. Figure 10(a) shows the trajectory in the $\log T - \log \Sigma$ plane for the model with $L = 0.08 L_E$ at $r = 8 r_G$. The evolution proceeds along the inspiralling path from the initial, slightly perturbed, state to the asymptotic one with only very small changes in the temperature and surface density. (All of this, and the associated behaviour in the $\log \dot{m} - \log \Sigma$ plane, was hidden inside the filled squares in Figures 6, 7 and 8.) The corresponding time series is shown in Figure 10(b) where one can see oscillations being damped to zero amplitude.

6 Comments and conclusions

In this section, we would first like to comment on issues connected with our introduction of additional numerical diffusion. This was motivated by observing that, in our first calculations, the supposedly stable model with $L = 0.01 L_E$ did not remain unchanging but instead developed an instability in the region $3 - 6 r_G$ after 10 – 20 s of the evolution. This appeared first at around $4.7 - 4.8 r_G$ and grew rapidly, causing termination of the calculation. Figure 11 shows the velocity and surface-density profiles for the developed instability. This behaviour was not entirely unexpected since it was already known that additional global instabilities may be introduced as a direct consequence of literal adoption of the Shakura/Sunyaev α viscosity prescription (see, for example, Abramowicz, Papaloizou and Szuszkiewicz, 1993). However, it was important to be sure that the behaviour seen was not merely an artefact of our numerical scheme and so we carried out several experiments to check on this including using an implicit method for the radial velocity equation and a three-point formula for the pressure gradient (the regridding procedure had already been subjected to extensive testing). The instability persisted unchanged in each case. Another set of experiments was carried out to test the effect of varying the viscosity parameter α . The instability was always present but appeared at different locations and after different times. We also tried different viscosity formulations but found that the instability was always present. F. Honma (private communication) has performed a calculation for the same model with his code but did not find the same behaviour. Our suspicion is that the discrepancy arises because of the fact that our basic code is very non-diffusive and, bearing in mind that the standard slim-disc model does not include several potentially important diffusive terms, we decided to try adding a low level of numerical diffusion to the radial equation of motion, as discussed earlier. We found that the instability was suppressed even with extremely small values of k , suggesting that the additional diffusive terms discussed in Section 2, but not included in the present formulation, probably play a crucial role for avoiding this instability which would otherwise make these models unsuitable as representations of real astrophysical discs. Since we wanted to focus on the more interesting non-stationary behaviour described in the main part of this paper, we included the additional diffusion for all of our calculations to avoid them being terminated prematurely. Without doing this, all of our sub-Eddington models suffer in the same way as the one with $L = 0.01 L_E$ but no similar behaviour is seen for super-Eddington models. We emphasize that the kind of numerical scheme which we are using here has been extensively tested for a wide range of physical situations and does not normally require the addition of extra numerical diffusion to give stable behaviour in circumstances such as these.

The aim of this paper has been to study the nonlinear evolution of the thermal instability for the original version of the slim disc model and to verify predictions concerning the stabilizing effect of advection. Setting aside the instability discussed in the previous paragraph, we have found that models predicted to be stable by local analysis do remain stable and stationary. The same applies for models which, according to the local analysis, would have a potentially unstable region smaller than the minimum wavelength for unstable perturbations. In terms of luminosities, this means that all models with luminosity less than or equal to $0.08 L_E$ are globally stable. For models with luminosities between $0.09 L_E$ and $1 L_E$, we see the run ended by unstable behaviour near to the sonic point.

For the models studied here and the particular formulation adopted, it seems very unlikely that advection alone can be sufficient to allow for the existence of limit cycle behaviour. Non-local effects which are not included here (such as radiative diffusion in the radial direction) might well play important role in the global evolution of the thermal instability since they introduce parabolic terms which could significantly affect the delicate radial force-balance.

Our results are rather different from those reported by the Japanese group (HMK). However, it should be emphasized that they used a viscosity parameter two orders of magnitude larger than ours and this gives rise to models which are very different from the original slim disc formulation which we have been studying here. In particular, it means that they are dealing with much larger radial velocities and hence the effect of advection is much stronger. We are currently in the process of investigating models with larger α .

In our future work, we plan to follow the programme outlined at the beginning of the paper: namely, to use the present study as a standard against which to judge the effects of systematically adding further sophistications onto the original slim disc formulation. Also, we have been studying super-Eddington models. A global analysis is really essential for discussing the stability of these since the local approximation is rather poor in this case. However, some qualitative predictions have been made on the basis of local analysis (Abramowicz et al. 1988, Wallinder 1991) and it will be interesting to compare them with the calculated global behaviour.

Acknowledgments

We would like to thank Marek Abramowicz, Bożena Czerny, Fumio Honma, Shoji Kato, Ryoji Matsumoto and John Papaloizou for some very interesting discussions about our results.

We gratefully acknowledge financial support from the U.K. Particle Physics and Astronomy Research Council and the Italian Ministero dell'Università e della Ricerca Scientifica e Tecnologica.

References

- Abramowicz, M.A., Czerny, B., Lasota, J-P., Szuszkiewicz, E., 1988, ApJ, 332, 646
- Abramowicz, M.A., Kato, S., Matsumoto, R., 1989, PASJ, 41, 1215
- Abramowicz, M.A., Papaloizou, J.C.B., Szuszkiewicz, E., 1993, Geophys. Astrophys. Fluid Dyn., 70, 215
- Chen, X., Taam, R.E., 1993, ApJ, 412, 254
- Chen, X., Taam, R.E., 1994, ApJ, 431, 732
- Cox, A.N., Stewart, J.N., 1970, ApJ Suppl., 19, 243
- Honma, F., Matsumoto, R., Kato, S., 1991, PASJ, 43, 147
- Honma, F., Matsumoto, R., Kato, S., Abramowicz, M.A., 1991, PASJ, 43, 147
- Hoshi, R., 1977, Prog. Theor. Phys., 58, 1191
- Kato, S., Abramowicz, M.A., Chen, X., 1996, PASJ, 48, 67
- Lasota, J.-P., Pelat, D., 1991, A&A, 249, 574
- Lightman, A.P., 1974, ApJ, 194, 429
- Lightman, A.P., Eardley, D.M., 1974, ApJ, 187, L1
- Loska, Z., 1982, Acta Astron., 32, 13
- Matsumoto, R., Kato, S., Honma, F., 1989, in Meyer, F., Duschl, W.J., Frank, J., Meyer-Hofmeister, E., eds, Theory of Accretion Disks. Kluwer Academic Publications, London, p. 167
- Meyer, F., and Meyer-Hofmeister, E., 1982, A&A, 106, 34
- Miller, J.C., Pantano, O., 1990, Phys. Rev. D, 42, 3334
- Muchotrzeb, B., Paczyński, B., 1982, Acta Astron., 32, 1
- Paczyński, B., 1980, Acta Astron., 30, 347
- Paczyński, B., Bisnovatyi-Kogan G., 1980, Acta Astron., 31, 283
- Paczyński, B., Wiita, P.J., 1980, A&A, 88, 23
- Papaloizou, J.C.B., Faulkner, J., Lin, D.N.C., 1983, MNRAS, 205, 487
- Papaloizou, J.C.B., Stanley, G.Q.G., 1986, MNRAS, 220, 593
- Papaloizou, J.C.B., Szuszkiewicz, E., 1994, MNRAS, 268, 29
- Piran, T., 1978, ApJ, 221, 652
- Pringle, J.E., 1976, MNRAS, 177,65

Pringle, J.E., 1981, *Ann. Rev. Astron. Astrophys.*, 19, 137
Pringle, J.E., Rees, M.J., Pacholczyk, A.G., 1973, *A&A*, 29, 179
Shakura, N.I., Sunyaev, R.A., 1973, *A&A*, 24, 337
Shakura, N.I., Sunyaev, R.A., 1976, *MNRAS*, 175, 613
Smak, J., 1982, *Acta Astron.*, 32, 199
Szuszkiewicz, E., 1988, Ph.D. Thesis, SISSA, Trieste
Szuszkiewicz, E., 1990, *MNRAS*, 244, 377
Taam, R.E., Lin, D.N.C., 1984, *ApJ*, 287, 761
Wallinder, F.H., 1991, *A&A*, 249, 107

Table 1: Results from local stability analysis of the initial models and the total physical time for which each model was evolved.

L/L_E	r_{sonic} [r_G]	unstable region [r_G]	Λ_{min} [r_G]	$r(\tau_{min})$ [r_G]	τ_{min} [s]	t_{calc} [s]
0.01	2.96	stable everywhere				
0.07	2.95	6.2 - 9.7	28.6	7.4	226	> 5650
0.08	2.95	5.3 - 12.8	7.7	6.6	56.8	> 7120
0.09	2.95	4.9 - 15.2	4.7	6.3	33.4	582
0.1	2.94	4.6 - 17.5	3.6	5.9	24.3	182
0.2	2.94	3.8 - 37.1	1.6	4.8	8.5	71
0.4	2.93	3.4 - 70.7	1.1	4.1	5.1	126
0.5	2.93	3.3 - 86.1	1.0	3.9	4.5	155
0.6	2.92	3.3 - 100.8	0.9	3.7	4.0	165
0.7	2.92	3.2 - 115.1	0.8	3.5	3.6	135
0.8	2.91	3.1 - 129.0	0.7	3.4	3.3	25
1.0	2.82	2.9 - 155.8	0.5	3.1	2.7	0.08

Figure Captions

Figure 1: Mach number (v_r/c_s) plotted as a function of r/r_G for the model with $L = 0.1 L_E$ at several different times: $t = 0$ s (dotted line), $t = 150$ s (short-dashed line), $t = 162$ s (long-dashed line), $t = 171$ s (dot/short-dashed line), $t = 178$ s (dot/long-dashed line), and $t = 180$ s (solid line).

Figure 2: Temperature T (in degrees Kelvin) plotted as a function of r/r_G for the model with $L = 0.1 L_E$ at several different times. The line description is the same as for Figure 1.

Figure 3: Surface density Σ (in g/cm^2) plotted as a function of r/r_G for the model with $L = 0.1 L_E$ at several different times. The line description is the same as for Figure 1.

Figure 4: The half-thickness of the disc, H (in cm) plotted as a function of r/r_G for the model with $L = 0.1 L_E$ at several different times. The line description is the same as for Figure 1.

Figure 5: Development of the instability near to the sonic point ($v_r/c_s = -1$) shown in terms of the Mach number. The model concerned is again the one with $L = 0.1 L_E$. The dotted line shows the initial Mach number profile and the rapid growth of the sharp-peaked structure is shown by profiles for three consecutive output times: $t = 180.2001$ s, 180.2028 s and 180.2069 s.

Figure 6: The $\log \dot{m} - \log \Sigma$ plane for $r = 8 r_G$ showing the location of the sequence of stationary models (dotted line) and the evolutionary paths (solid and dashed lines) for models with $\dot{m} = 0.01, 0.07, 0.08, 0.2, 1$ and 10 . The initial location for each model is marked by an open square and the final position is marked by a filled square. See text for a more detailed description.

Figure 7: The left-hand column shows the $\log \dot{m} - \log \Sigma$ plane for four different radii: (a) $3 r_G$, (b) $5 r_G$, (c) $8 r_G$ and (d) $10 r_G$. The evolutionary paths are for the same models as in Fig. 6 except that $\dot{m} = 0.2$ is replaced by $\dot{m} = 0.1$. The right-hand column (figures (e) – (h)) shows the corresponding behaviour in the $\log T - \log \Sigma$ plane.

Figure 8: The $\log \dot{m} - \log \Sigma$ plane for $3 r_G$ (left-hand column) and $5 r_G$ (right-hand column) for three different models: (a) $\dot{m} = 0.2$, (b) $\dot{m} = 0.4$ and (c) $\dot{m} = 0.8$.

Figure 9: (a) The evolutionary paths in the $\log T - \log \Sigma$ plane for $r = 8 r_G$ for models with $\dot{m} = 0.09$ (solid line) and 0.1 (dashed line). The S-curve is shown by the dotted line. (b) The time variation of the temperature at $r = 8 r_G$ for the model with $\dot{m} = 0.09$.

Figure 10: (a) The evolutionary path in the $\log T - \log \Sigma$ plane for $r = 8 r_G$ for the model with $\dot{m} = 0.08$. The S-curve is shown by the dotted line. (b) The time variation of the temperature at $r = 8 r_G$ for the model with $\dot{m} = 0.08$.

Figure 11: The profiles of (a) Mach number and (b) surface density for the model with $\dot{m} = 0.01$ at three different times: $t = 0$ s (dashed line), $t = 76$ s (lower amplitude perturbation) and $t = 87.7$ s (higher amplitude perturbation).

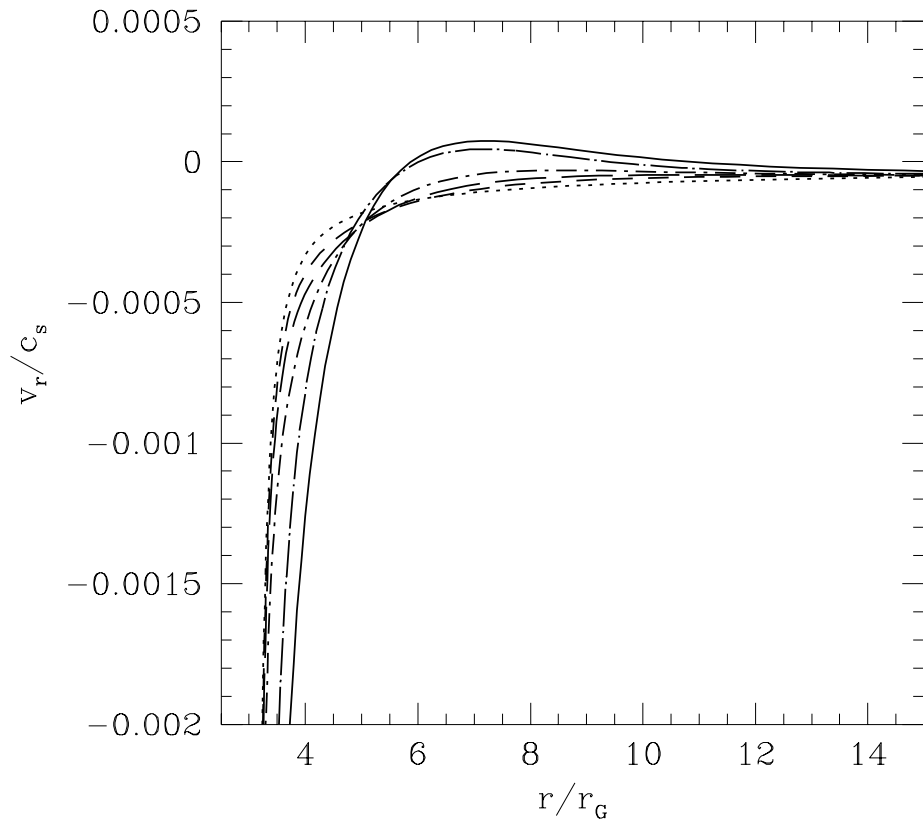


Figure 1

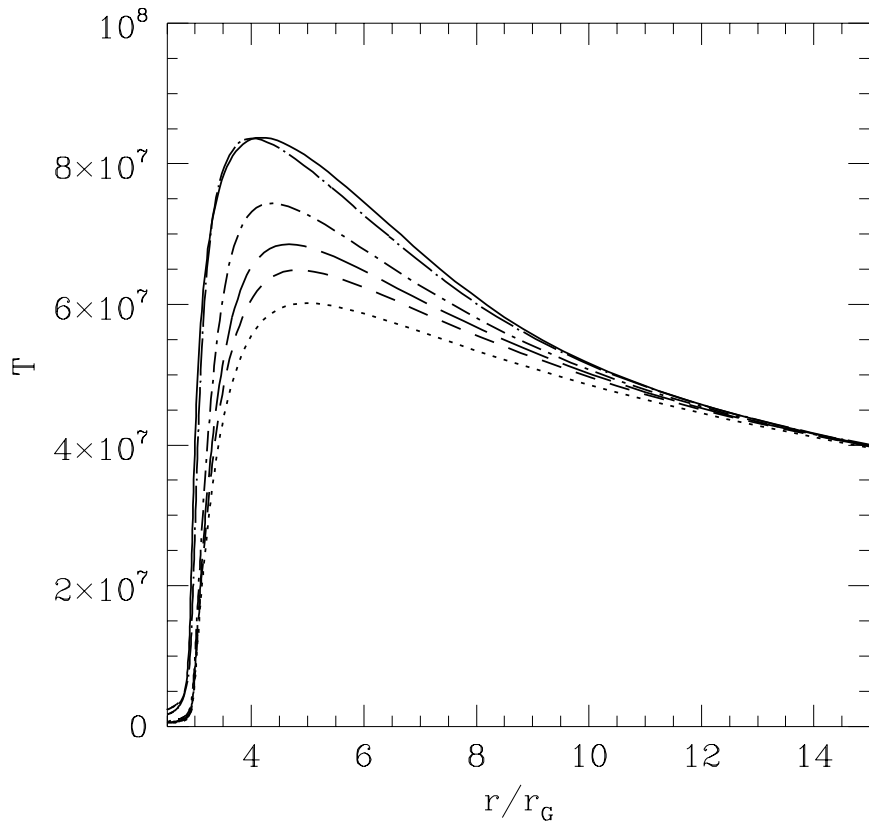


Figure 2

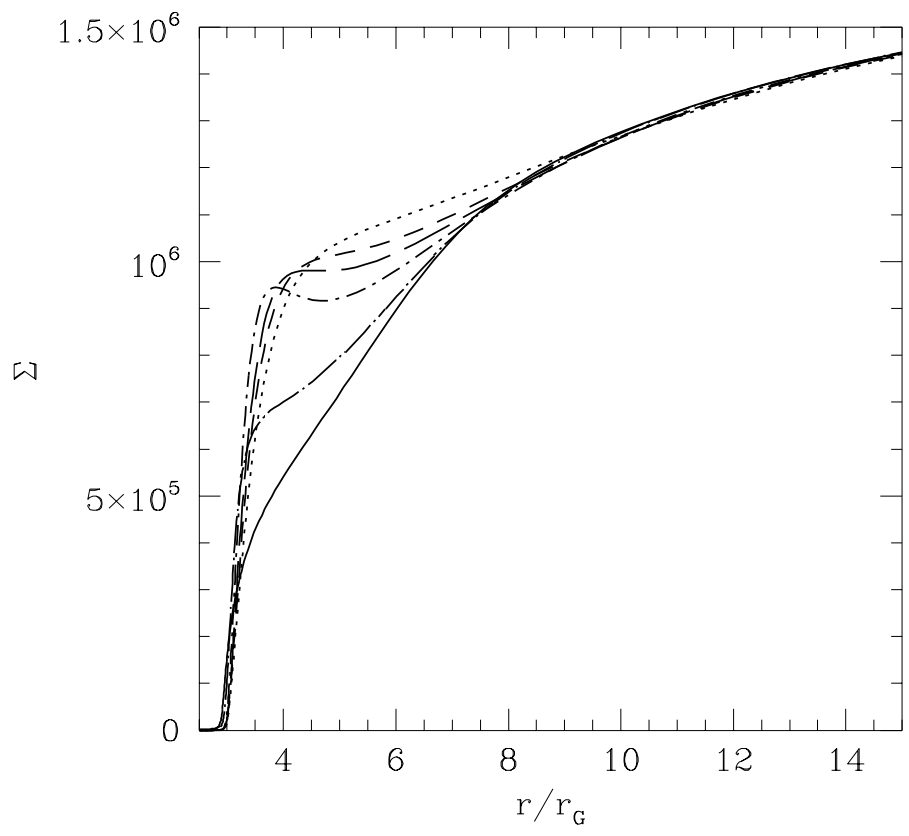


Figure 3

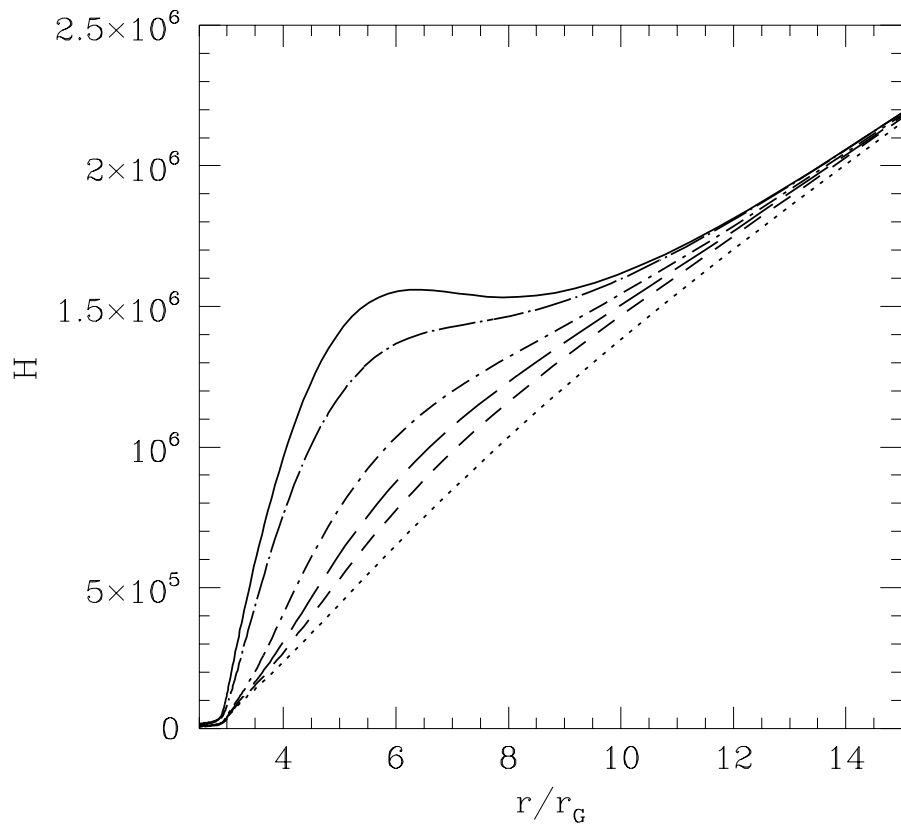


Figure 4

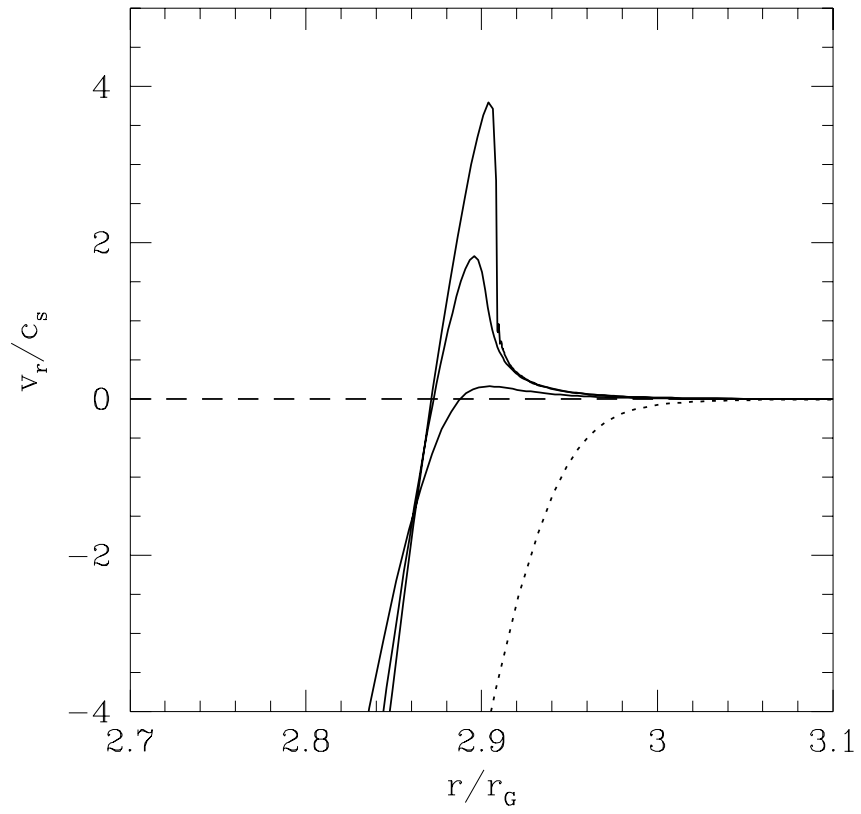


Figure 5

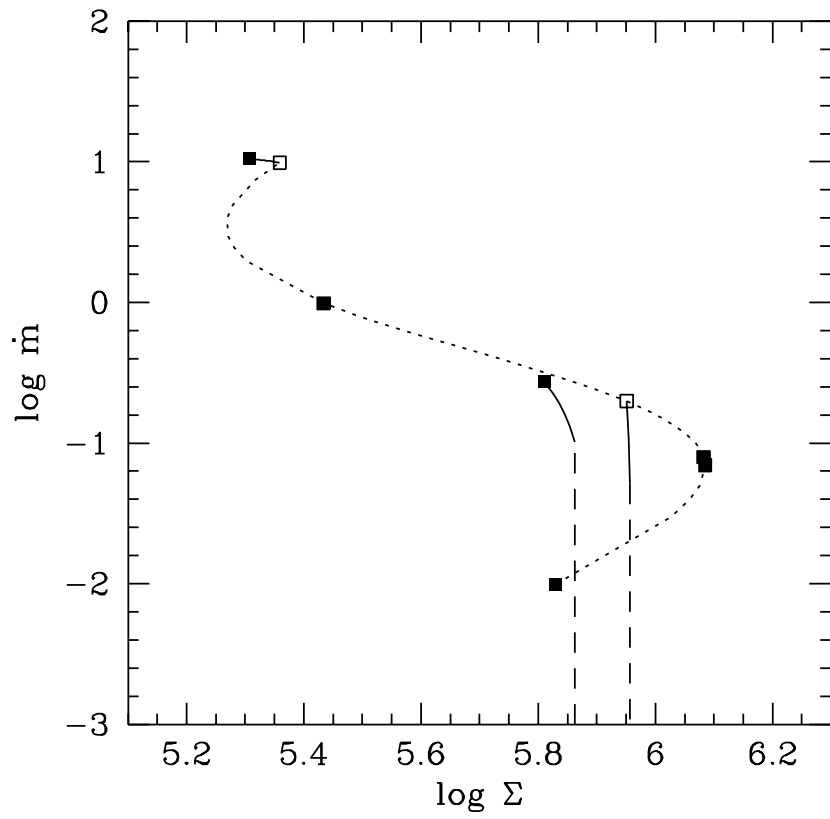


Figure 6

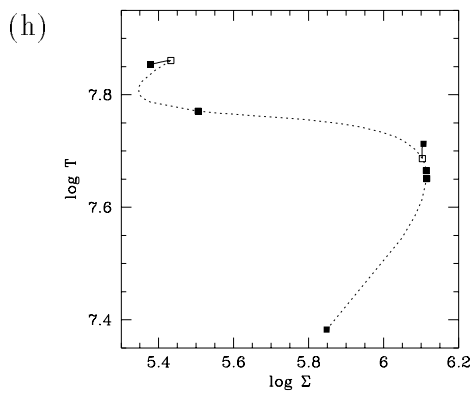
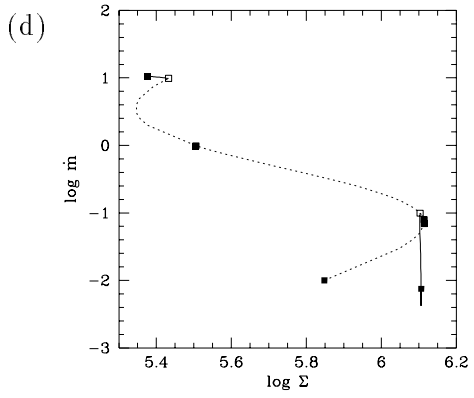
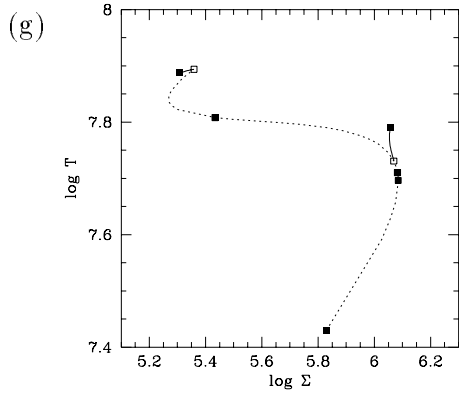
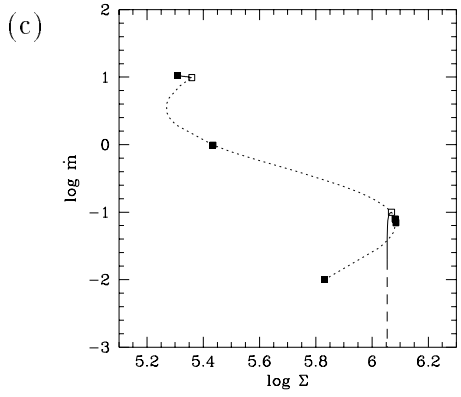
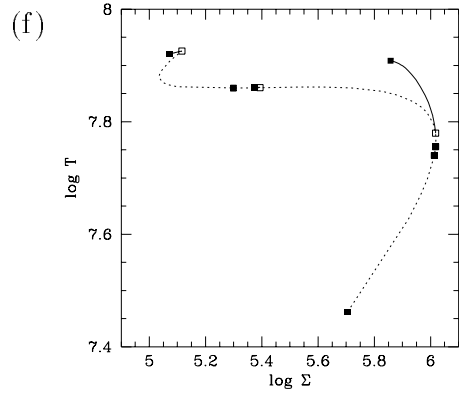
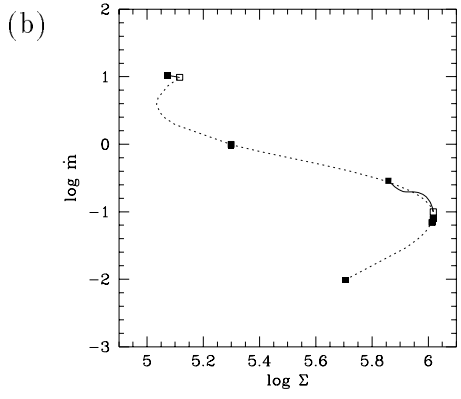
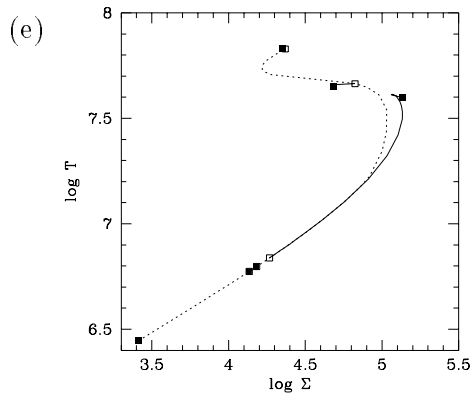
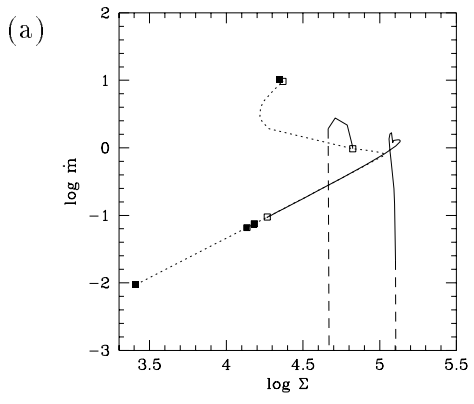


Figure 7

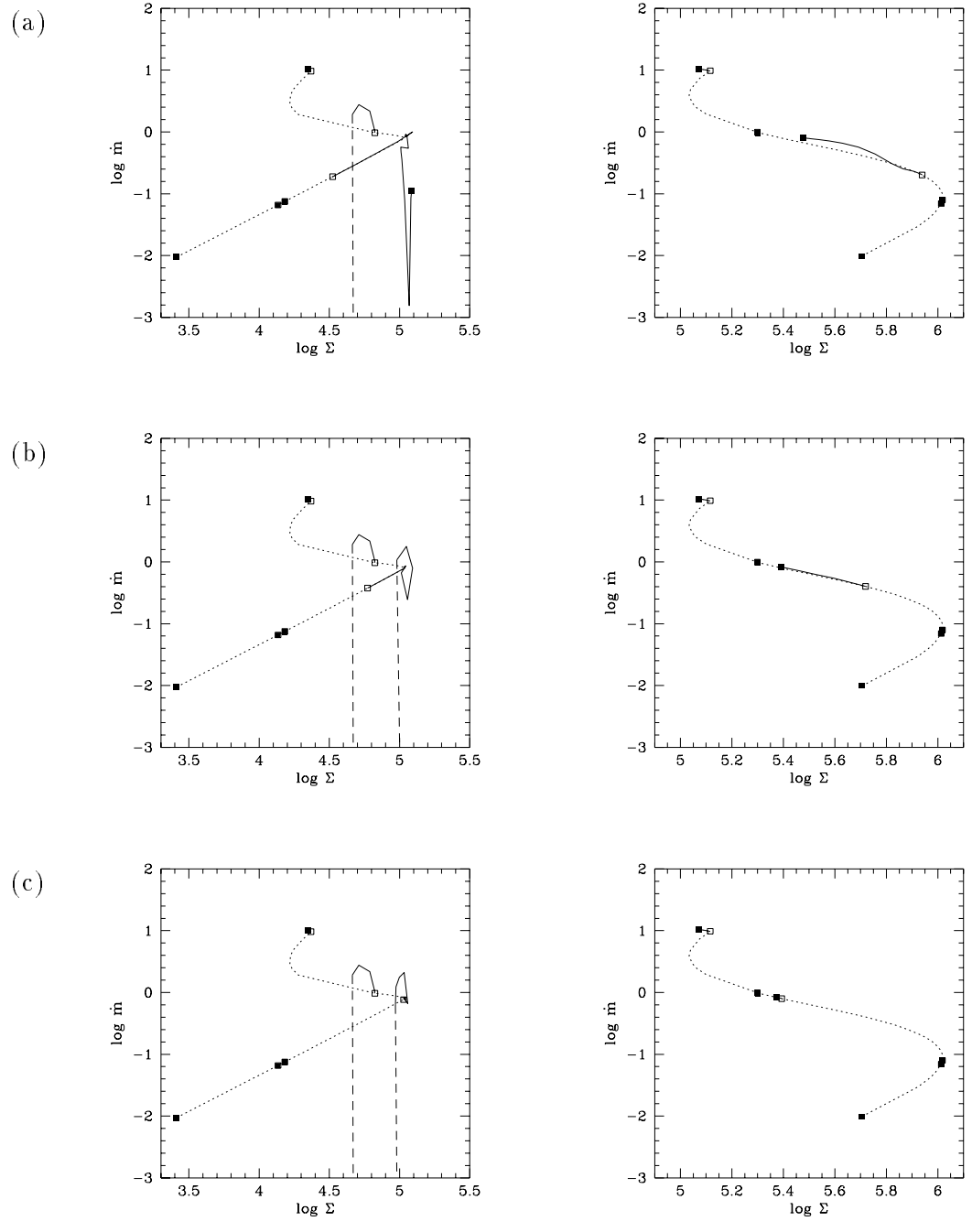


Figure 8

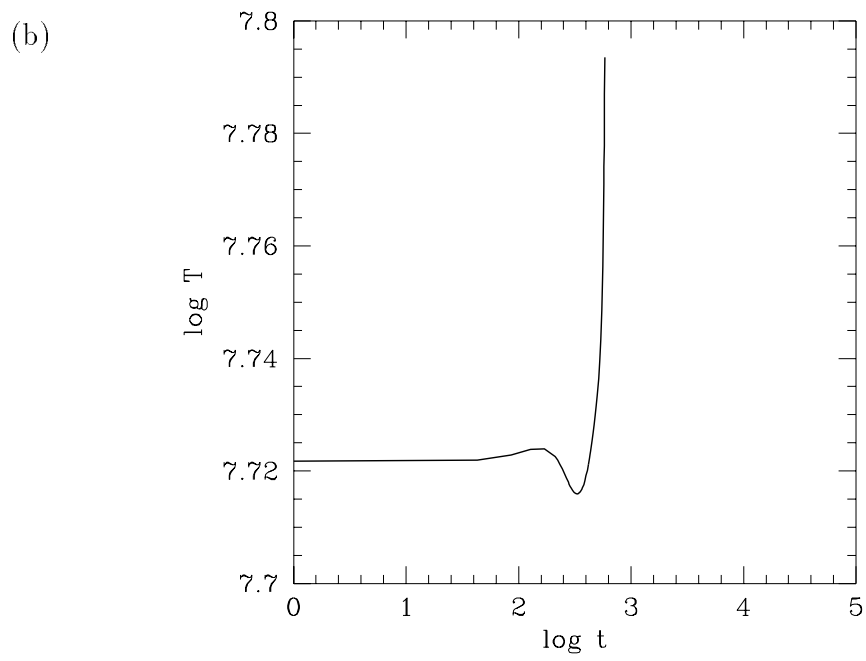
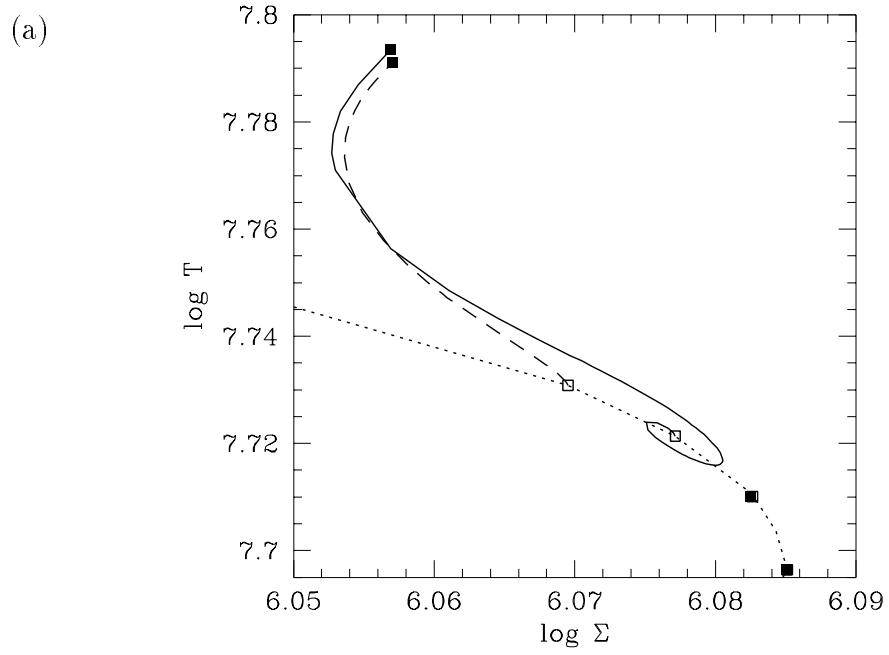


Figure 9

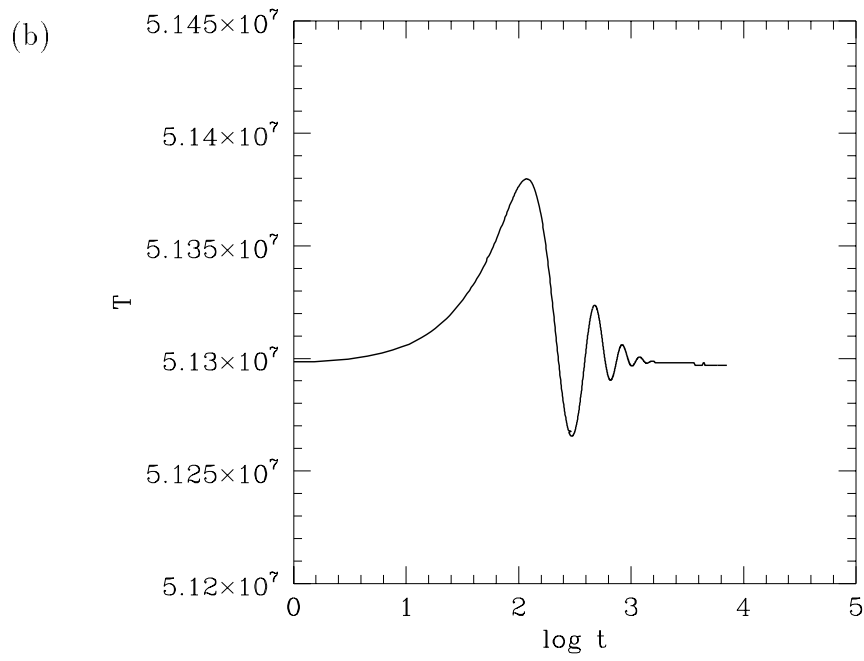
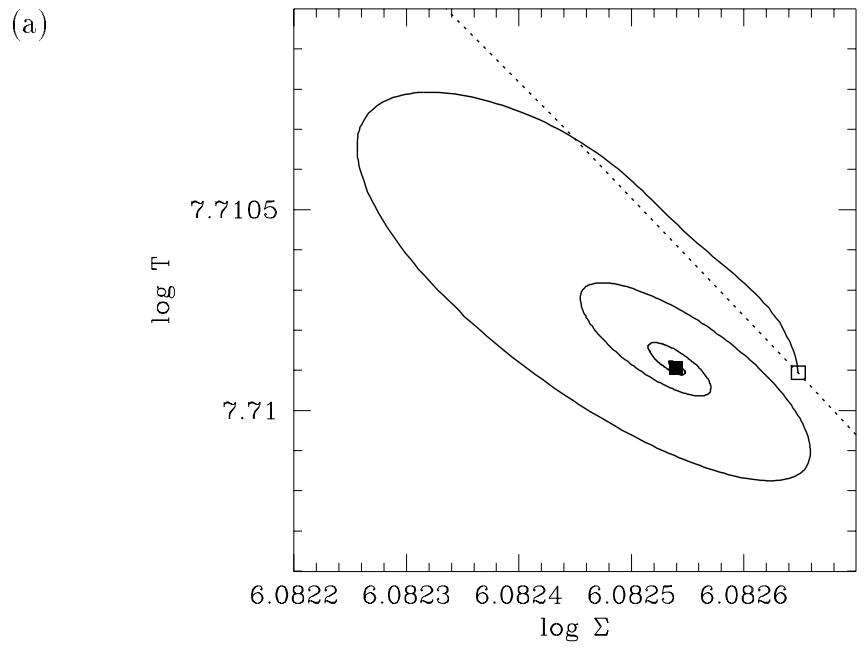


Figure 10

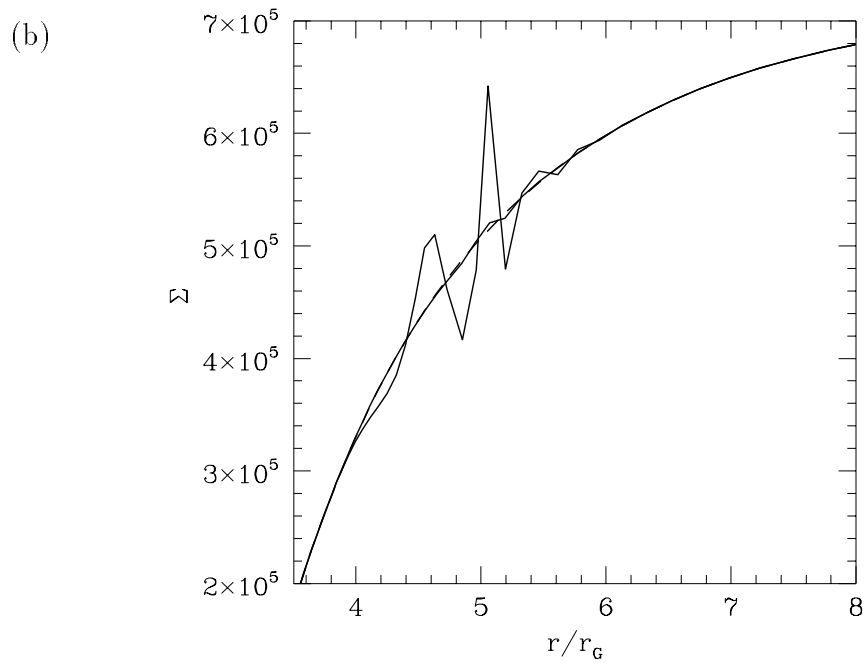
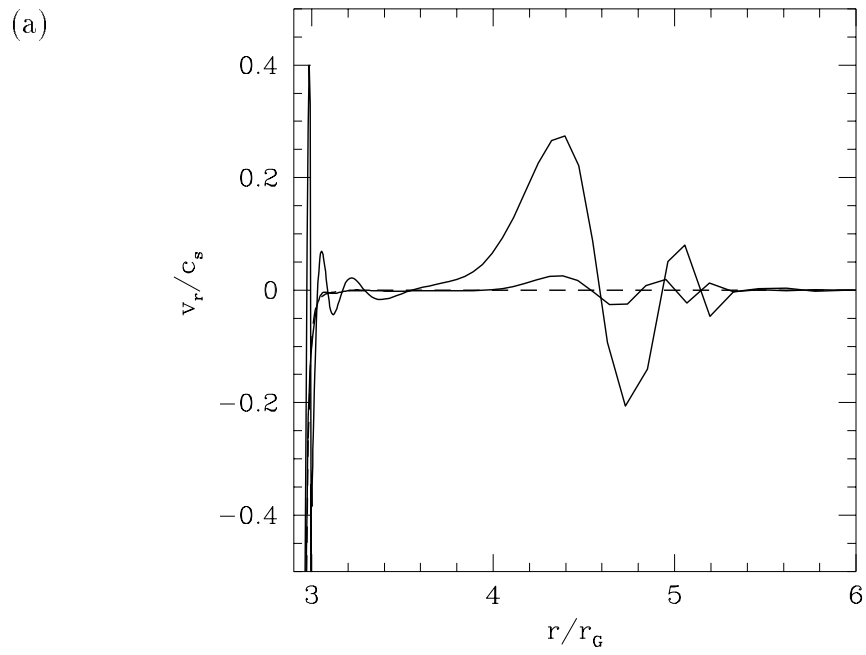


Figure 11